

Physics-Regularized Multi-Modal Image Assimilation for Brain Tumor Localization

Michal Balcerak^{1*}, Tamaz Amiranashvili^{1,2}, Andreas Wagner²,
Jonas Weidner², Petr Karnakov³, Johannes C. Paetzold⁴, Ivan Ezhov²,
Petros Koumoutsakos³, Benedikt Wiestler^{2†}, Bjoern Menze^{1†}

¹University of Zurich, ²Technical University of Munich
³Harvard University, ⁴Imperial College London

Abstract

Physical models in the form of partial differential equations represent an important prior for many under-constrained problems. One example of such uses is tumor treatment planning, which heavily depends on an accurate estimate of the spatial distribution of tumor cells in a patient’s anatomy. Medical imaging scans can identify the bulk of the tumor, but they cannot reveal its full spatial distribution. Tumor cells at low concentrations remain undetectable, for example, in the most frequent type of primary brain tumors, glioblastoma. Deep-learning based approaches fail to estimate the complete tumor cell distribution due to a lack of reliable training data. Most existing works therefore rely on physics-based simulations to match observed tumors, providing anatomically and physiologically plausible estimations. However, these approaches struggle with complex and unknown initial conditions and are limited by overly rigid physical models. In this work, we present a novel method that allows balancing data-driven and physics-based cost functions. In particular, we propose a unique discretization scheme that allows quantifying the adherence of our learned spatiotemporal tumor and brain tissue distributions to their corresponding growth and elasticity equations. This quantification, serving as a regularization term rather than a hard constraint, enables greater flexibility and proficiency in assimilating patient data than existing models. We demonstrate improved coverage of tumor recurrence areas compared to existing techniques on real-world data from a cohort of patients. The method brings the potential to enhance clinical adoption of model-driven treatment planning for glioblastoma.

1 Introduction

The management of gliomas, notably glioblastomas, is highly challenging due to their infiltration beyond the tumor margins visible in medical scans such as Magnetic Resonance Imaging (MRI). This characteristic significantly complicates the accurate personalization of radiotherapy. Current clinical practices apply uniform distance margins around the visible tumor on MRI scans to target the full spatial distribution of tumor cells. However, these practices do not utilize our knowledge of infiltration patterns, tissue-specific characteristics, and anatomical barriers, thereby failing to capture the complex dynamics of individual tumor spread. Effectively tailoring radiotherapy to an individual patient’s tumor’s spread is an unmet clinical need in neurooncology [1].

To address this challenge, two main computational approaches have emerged:

*Corresponding author: michal.balcerak@uzh.ch

†Contributed equally as senior authors.

Hard-Constrained Physics-Based Models: These models use Partial Differential Equations (PDEs) to constrain the solution space, ensuring that output tumor cell distributions adhere strictly to predefined physical laws [2, 3, 4, 5]. However, since PDEs are only approximations of the underlying stochastic processes in complex biological environments, they can overconstrain the system. While such models can be informative and structured, they cannot capture the complex behaviors intrinsic to biological processes like tumor growth. Consequently, the data cannot be fully assimilated due to these restrictions, leading to a limited utility of the physical models in representing empirical data.

Data-Driven Models: These models [6, 7] offer great flexibility by leveraging access to imaging datasets. However, they often lack rigorous quality control and fail to integrate crucial biological insights, such as tissue-specific infiltration patterns and brain topology. This makes them less reliable for clinical application, especially when there is insufficient data to infer them purely from imaging information.

Combining physical insights on spatiotemporal distributions with increased model flexibility could be highly beneficial. One approach to achieve this is by testing the physics residual in selected locations, as demonstrated in Physics-Informed Neural Networks (PINNs) [8, 9, 10, 11, 12]. Another way involves projecting the learned solution into a latent space that adheres to physics constraints [13, 14]. A different framework, Optimizing a Discrete Loss (ODIL) [15], constructs a residual of PDEs using grid-based discretization. Unlike methods that optimize neural network parameters, ODIL directly optimizes the discretized unknown fields

Both ODIL [16] and PINNs [17] have recently been employed to model growth equations conditioned on MRI and FET-PET imaging of patients. ODIL advances state-of-the-art radiotherapy planning by relaxing the constraints of the growth equation, thereby enhancing the capture of tumor recurrence. A similar trend is observed in computer vision’s novel view synthesis, where neural radiance field MLPs [18] are being replaced by discrete representations [19, 20, 21].

However, these approaches do not account for brain tissues as part of the dynamics and do not utilize the information available in the imaging data regarding visible anatomical deformations. Incorporating tissue elasticity is challenging because the exact initial anatomy is unknown, and the dynamics themselves are computationally challenging due to the significantly increased number of unknown fields. Thus, no hybrid approach free from hard PDE constraints has yet successfully connected biological processes, such as tumor growth, with models of its biological environment, such as the tissue elasticity models. Very few works have been done [22, 23] using PINNs for biomechanical modeling only on synthetic scenarios, demonstrating that the displacement field of materials can be learned from observations.

The main contributions of this work are as follows:

- We construct discrete physics-based residuals for both the tumor growth and the biomechanical processes of dynamic tissues from the Lagrangian perspective of particles that carry tissue intensities. Eulerian projections on static grids are used to condition the learnable tumor cell and tissue distributions on available visible observations. Unlike data-driven models, our method remains robust due to physics regularization while being more flexible at adapting data than hard-constrained numerical simulations.
- Our method allows for the estimation of the initial condition of the biomechanical environment. We demonstrate the ability to learn the complex unknown initial condition, which, in our case, is not just the origin of the pathology but also the initial state of the brain tissue anatomy.
- We validate our method* on the downstream task of radiotherapy planning using the largest publicly available dataset known to us, achieving new state-of-the-art performance in capturing tumor recurrence.

*GitHub: <https://github.com/m1balcerak/PhysRegTumor>

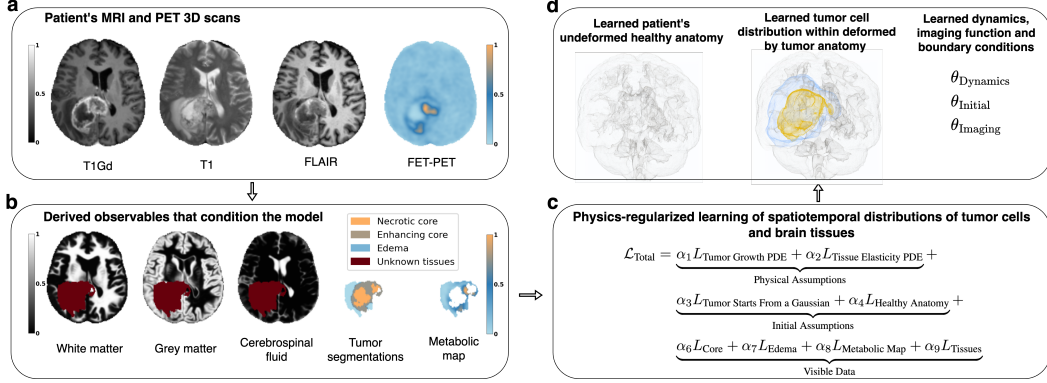


Figure 1: Method overview. (a) 3D MRI and PET scans of a glioblastoma patient (b) Preprocessed input includes brain tissue maps, tumor segmentation, and a metabolic map from FET-PET. (c) Tumor cell distribution and brain anatomy inferred using a loss function based on assumptions about physical processes, initial conditions. (d) Outcomes: initial healthy anatomy, spatial tumor cell distribution, and system identification parameters.

In Figure 1, we visualize an overview of our method, showing how we condition the learnable full spatial tumor cell distribution on the patient data and regularize it using soft assumptions about the physics of tumor growth, tissue elasticity, and initial conditions for both the anatomy and the tumor. In addition to multiparametric MRI scans (T1Gd, T1, FLAIR), we incorporate Fluoroethyl-L-tyrosine PET (FET-PET), a specialized form of Positron Emission Tomography (PET), as an additional imaging modality that captures the metabolic activity of tumor cells.

2 Physical Assumptions

Our model integrates physical assumptions to ensure that the learned tumor cell distribution adheres to established biological and mechanical principles. These assumptions are incorporated into the loss function as regularization terms alongside initial condition assumptions and data terms.

2.1 Physical Model

We consider the problem of learning the tumor cell distribution within the domain $\Omega \times (0, 1]$, where $(0, 1]$ represents the assumed time of tumor growth, and the unit cube $\Omega = [0, 1]^3$ describes our spatial domain.

The objective is to determine a tumor cell density function $c(x, t)$, $(x, t) \in \Omega \times (0, 1]$ approximately satisfying the reaction-diffusion-advection equation [24]:

$$\frac{\partial c}{\partial t} = \underbrace{\mathcal{D}c}_{\text{cell migration through diffusion}} + \underbrace{\mathcal{S}c}_{\text{cell proliferation}} - \underbrace{\nabla \cdot (vc)}_{\text{tissue displacements through advection}}, \quad (1)$$

where $\mathcal{D}c = \nabla \cdot (D(\mathbf{m})\nabla c)$ represents the diffusion of the cells with the tissue-dependent diffusion constant $D(\mathbf{m})$, $\mathcal{S}(c) = \rho c(1 - c)$ describes the cell growth with a growth factor ρ , and \mathbf{v} is a velocity field moving the cells in the interior of the domain due to the tissue's elastic properties and the tumor-induced stresses in the tissue.

The brain tissue vector \mathbf{m} , which represents the percentage-wise concentration of different tissue types, is defined as $\mathbf{m}(x, t) = [m_{\text{WM}}(x, t), m_{\text{GM}}(x, t), m_{\text{CSF}}(x, t)]$, where m_{WM} , m_{GM} , and m_{CSF} denote the concentrations of white matter, gray matter, and cerebrospinal fluid, respectively.

The brain tissue vector \mathbf{m} is governed by

$$\partial_t \mathbf{m} + \text{div}(\mathbf{m} \otimes \mathbf{v}) = 0, \quad (2)$$

where \otimes denotes the outer product. We assume Neumann boundary conditions for both c and \mathbf{m} . For c , the no-flux condition applies at the borders of diffusive tissues, specifically the combined white

and gray matter. For each tissue component in \mathbf{m} , the no-flux boundary is assumed to be the constant brain boundary visible in the MRI scans.

The tumor induced stresses lead to a displacement field \mathbf{u} , such that the velocity is given by $\mathbf{v} = \partial_t \mathbf{u}$. We assume quasi-static mechanical equilibrium due to the slow tumor growth rate relative to tissue mechanical responses, leading to

$$\nabla \cdot \boldsymbol{\sigma}(\mathbf{u}) + \gamma \nabla c = 0, \quad (3)$$

where γ regulates the impact of the tumor on the displacement and is a learnable patient-specific parameter. We apply the Neo-Hookean model [25] to represent hyperelastic behavior in biological tissues, where the stress $\boldsymbol{\sigma}$ is related to the deformation gradient $\mathbf{F}_{ij} = \delta_{ij} + \frac{\partial u_i}{\partial x_j}$ with the Lamé parameters λ and μ (material properties in Appendix E), averaged across different tissue types to accommodate the heterogeneity:

$$\boldsymbol{\sigma} = \frac{\bar{\mu}}{J}(\mathbf{F}\mathbf{F}^T - \mathbf{I}) + \bar{\lambda} \ln(J)\mathbf{I}, \quad (4)$$

with $J = \det(\mathbf{F})$. The averaged Lamé parameters, $\bar{\lambda}$ and $\bar{\mu}$, are computed based on the proportional contributions of constituent tissues, ensuring the stress tensor accurately reflects the composite mechanical properties of the mixed tissues. This methodology facilitates detailed simulations adhering to the elasticity laws relevant to heterogeneous biological environments.

The set of learnable parameters θ_{Dynamics} describing the tumor dynamics, is thus given by $\theta_{\text{Dynamics}} = \{D_{\text{GM}}, R, \rho, \gamma\}$, where D_{GM} and $D_{\text{WM}} = R D_{\text{GM}}$ are the diffusivities in pure gray and white matter regions, which are averaged to the effective diffusivity with a weighted average based on the tissue proportions.

2.2 Discrete Physics Residuals

We use two different approaches to discretize the elasticity equations and the reaction-diffusion-advection equations. For the former, we use a time-dependent grid in space, described by the N_x points $(\mathbf{p}_j^n)_{1 \leq j \leq N_x}$ at time $n\Delta t$, $0 \leq n \leq N_t$, which initially form a uniform grid on Ω . For the latter, we further partition the domain Ω at the n th point in time into N_x cells Ω_i^n , $1 \leq i \leq N_x$, such that $\Omega = \bigcup_{i=1}^{N_x} \Omega_i^n$. Note that the cell midpoints \mathbf{x}_j directly depend on the particle positions \mathbf{p}_j due to the tissue deformation and that the shape of the cells Ω_i is given by a Voronoi tessellation of \mathbf{x}_j .

The displacement field \mathbf{u}_j^n is computed based on the initial ($t = 0$) and current ($t = n\Delta t$) positions of particles \mathbf{p}^n within the tissue by $\mathbf{u}^n = \mathbf{p}^n - \mathbf{p}^0$. Using central finite differences on the initial uniform reference grid, we can consecutively approximate $\nabla \mathbf{u}_j^n$, \mathbf{F}_j^n , ∇c_j^n , $\nabla \cdot \boldsymbol{\sigma}_j^n$, and define the tissue residual

$$L_{\text{Tissue Elasticity PDE}} = \sum_{n=0}^{N_t} \sum_{j=0}^{N_x} (\nabla \cdot \boldsymbol{\sigma}_j^n + \gamma \nabla c_j^n)^2. \quad (5)$$

As the particles, representing grid points, move with the tissue's deformation, they inherently accommodate the advection. Thus, the observed displacement of tumor cells attributed to advection is absorbed into the changes in particle positions. This leads to a simplification of the tumor equation when solved in the moving reference frame of the particles.

We use an implicit Euler scheme combined with a cell-centered finite-volume discretization to discretize the tumor equation. We denote the boundaries between two cells $1 \leq i, j \leq N_x$ by $\Gamma_{ij}^n = \Gamma_{ji}^n = \partial\Omega_i^n \cap \partial\Omega_j^n$. Further, the index set of all neighboring cells of Ω_i^n is given by $N_i = \{j : \partial\Omega_j \cap \partial\Omega_i \neq \emptyset \wedge j \neq i\}$ and assumed to stay independent of n , due to the extend of our deformations (see limitations in Section 7). For a function c_i^n at time $n\Delta t$ at the i th cell, we discretize the diffusion \mathcal{D} and reaction \mathcal{S} operators by

$$\mathcal{D}[c_i^n, D_i^n] = \sum_{j \in N_i} |\Gamma_{ij}| D_{ij}^n \frac{c_j^n - c_i^n}{\|\mathbf{x}_j^n - \mathbf{x}_i^n\|}, \text{ and } \mathcal{S}[u_i^n] = |\Omega_i^n| \rho c_i^n (1 - c_i^n), \quad (6)$$

where D_{ij}^n is the harmonic mean of D^n at the cell boundary, $|\Gamma_{ij}^n|$ denotes the interface area, and $|\Omega_i^n|$ denotes the cell volume. We thus obtain the tumor loss by

$$L_{\text{Tumor Growth PDE}} = \sum_{n=0}^{N_t} \sum_{j=0}^{N_x} \left(\frac{|\Omega_i^n|}{\Delta t} (c_i^n - c_i^{n-1}) - \mathcal{D}[c^n, D^n] - \mathcal{S}[c^n] \right)^2. \quad (7)$$

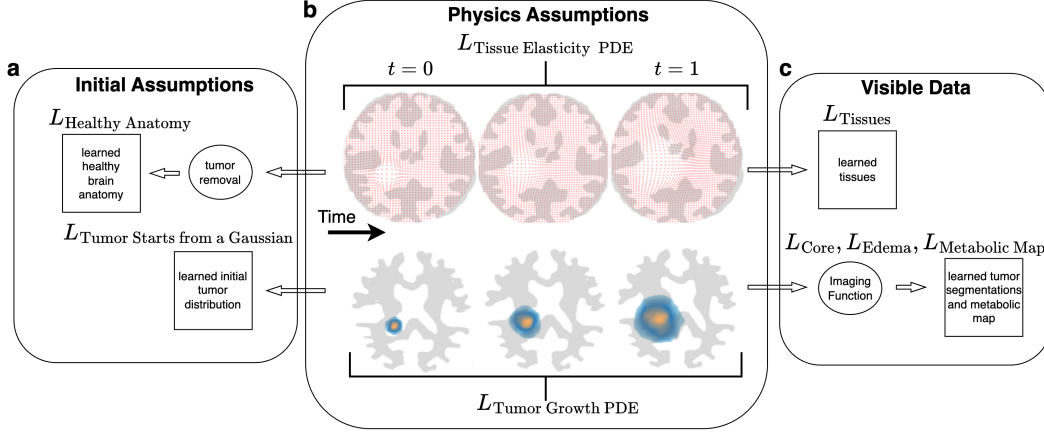


Figure 2: Learning process overview: optimization of spatiotemporal distributions of tumor cells and tissues. (a) Initial condition penalties enforce symmetric healthy anatomy, with the initial tumor distribution at $t = 0$ as a Gaussian. (b) Physics penalties regularize dynamics between $t = 0$ and t_{Final} . The first row shows gray matter contours with particle positions; the second row shows white matter contours with learned tumor concentrations. (c) Agreement of tumor distribution with anatomical tissues, visible segmentations, and metabolic map after transforming the final tumor distribution through the imaging function.

2.3 Particle-Grid Projections

While a Lagrangian frame representation from the point of view of particles is beneficial for accurately modeling advection, an Eulerian frame is essential for rendering the advected particle states into the image space. Denoting the Eulerian and Lagrangian frames as G and P respectively, an Eulerian field \mathcal{F}^G and a Lagrangian field \mathcal{F}^P are related through:

$$\mathcal{F}_p^P \approx \sum_i w_{ip} \mathcal{F}_i^G, \quad \mathcal{F}_i^G \approx \frac{\sum_p w_{ip} \mathcal{F}_p^P}{\sum_p w_{ip}} \quad (8)$$

where i indexes grid nodes, p indexes particles, and w_{ip} represents the weight of the trilinear shape function defined on node i and evaluated at the location of particle p .

3 Initial Assumptions

To model the initial conditions of the tumor and brain tissues, we incorporate specific assumptions into our loss functions. These assumptions help to align the model with expected biological and anatomical conditions without the tumor and at the time of its origin.

3.1 Initial Tumor Distribution

We assume that the initial tumor distribution follows a Gaussian profile. This is represented by penalizing the difference between $\mathcal{F}^G(u)^0$ and a Gaussian function centered at $x_0 \in \Omega$. The center of this Gaussian profile, x_0 , is part of the learnable parameters $\theta_{\text{Initial}} = \{x_0, \mathbf{m}^0\}$. The initial condition loss $L_{\text{Tumor starts from a Gaussian}}$ is as defined as:

$$L_{\text{Tumor starts from a Gaussian}} = \sum_{i=0}^{N_x} \left(\mathcal{F}^G(c)_i^0 - D_1 \exp \left(-\frac{(x_i - x_0)^2}{D_2} \right) \right)^2 \quad (9)$$

where $D_1 = 0.5$ and $D_2 = 0.02$ are constants.

3.2 Healthy Anatomy

A healthy brain is roughly symmetric between hemispheres, as justified by anatomical and functional observations. Imaging techniques such as MRI reveal symmetrical tissue structures, and electroencephalography (EEG) recordings show symmetrical patterns of electrical activity in the brain [26, 27]. This assumption applies to key tissue types, including white matter, gray matter, and cerebrospinal fluid. Enforcing the symmetry condition at progressively coarser resolutions aids in convergence. We construct a loss function, denoted as $L_{\text{Healthy Anatomy}}$, to quantify the asymmetry of the learned $\mathcal{F}^G(\mathbf{m}^0)$. The implementation details are provided in Appendix C.

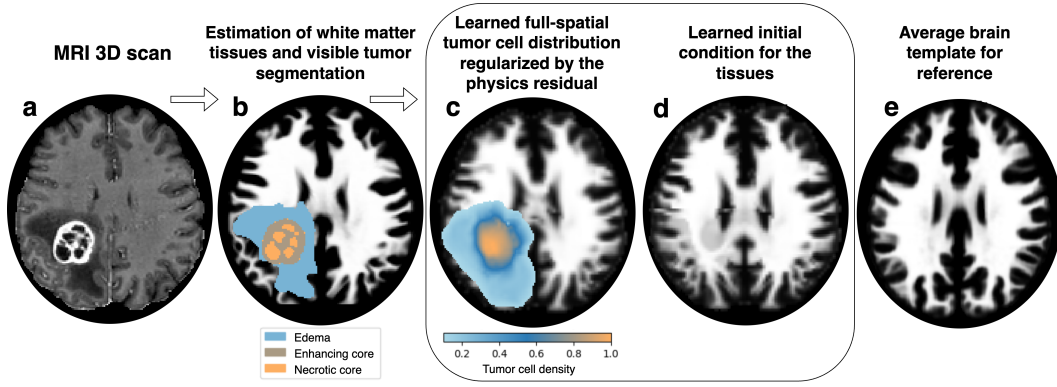


Figure 3: Inference overview. (a) Patient’s MRI 3D scans. (b) Estimated tissues through non-rigid registration of the average brain, showing white matter and visible tumor segmentations. (c) Learned tumor cell distribution, regularized by the physics residual and aligned with patient data. (d) Learned initial condition of the tissues representing healthy anatomy. (e) Average brain template for reference, rigidly registered to the MRI scan. Notable anatomical differences include the lack of matter passage between the hemispheres next to the tumor, which could affect tumor cell inference results.

4 Visible Data

Visible data refers to information directly observed from the patient’s MRI and FET-PET 3D scans, including visible tumor parts and surrounding brain tissues. As shown in Figure 1, this data includes estimated brain tissue probability maps, visible tumor segmentation, and a metabolic map derived from FET-PET scans, focusing on the enhancing core and edema. MRI scans provide segmentation maps [28], revealing the visible tumor. Using non-rigid atlas image registration with tumor masking [29], we estimate tissues both outside and hidden by the tumor, including white matter (WM), gray matter (GM), and cerebrospinal fluid (CSF). These observations offer partial information about both the anatomy and the tumor cell distribution.

The imaging function (see Figure 2) bridges simulated tumor cell densities with visible tumor segmentation and brain tissues, as well as the metabolic map. It depends on parameters for thresholding the tumor cell distribution to obtain segmentation, denoted as θ_{Imaging} , which must be learned.

We construct a loss function that minimizes the difference between model predictions and patient observables. Specifically, L_{Core} matches the visible tumor core, L_{Edema} matches the visible edema, and $L_{\text{Metabolic Map}}$ matches the metabolic map profile. Tissue intensities carried by particles are set to reproduce the patient’s estimated tissues at $t = 1$. While these intensities are predetermined, particle positions are weakly constrained, so matching the tissues (WM, GM, CSF) to the observed structures outside the tumor is enforced through L_{Tissues} . The constructed penalty terms align our spatiotemporal

distributions of tumor cells and tissues with patient data characteristics. Implementation details of the data losses and the imaging function are provided in Appendix B.

5 Combined Loss Function

The loss function $\mathcal{L}_{\text{Total}}$ is constructed to balance the contributions of physics-based regularization, assumptions about the initial conditions, and the visible empirical data. This facilitates a comprehensive approach to infer the full spatial tumor cell distribution at the time of the patient’s data acquisition (see Figure 3 for an overview of the inference process and Figure 2 for the learning process visualization):

$$\begin{aligned} \mathcal{L}_{\text{Total}} = & \underbrace{\alpha_1 L_{\text{Tumor Growth PDE}} + \alpha_2 L_{\text{Tissue Elasticity PDE}}}_{\text{Physical Assumptions}} + \\ & \underbrace{\alpha_3 L_{\text{Tumor Starts From a Gaussian}} + \alpha_4 L_{\text{Healthy Anatomy}}}_{\text{Initial Assumptions}} + \\ & \underbrace{\alpha_6 L_{\text{Core}} + \alpha_7 L_{\text{Edema}} + \alpha_8 L_{\text{Metabolic Map}} + \alpha_9 L_{\text{Tissues}}}_{\text{Visible Data}} \end{aligned} \quad (10)$$

All α_* parameters were selected through synthetic experiments with both single focal and local multi-focal tumors, as explained in Appendix D.

6 Validation and Ablation Study of Radiotherapy Planning

It is important to note that there is no objective ground truth for the tumor cell distribution of pre-operative tumors. The performances of methods are evaluated through the efficacy at a downstream task of predicting tumor recurrence present at a follow-up MRI scan within a volume defined by inferred tumor cell concentration[†] isosurfaces. The total volume of the region encompassed by the isosurfaces adheres to the current clinical practice, which uses a 1.5 cm distance isosurface around the pre-operative MRI-segmented tumor core, referred to as the Standard Plan, excluding any areas outside the brain tissues. Figure 4 visualizes the Standard Plan and a plan based on our learned tumor cell distribution. Each model’s target volume is simply a redistribution of the Standard Plan volume.

Our evaluation metric is *Recurrence Coverage* [%], which measures the percentage of the tumor segmentation, as detected on follow-up MRIs, that is encompassed within the radiotherapy target volume defined by each model. Additionally, follow-up MRI scans showing tumor recurrence are registered to the pre-operative anatomy using rigid registration, ensuring that predictions and actual recurrences are aligned accurately.

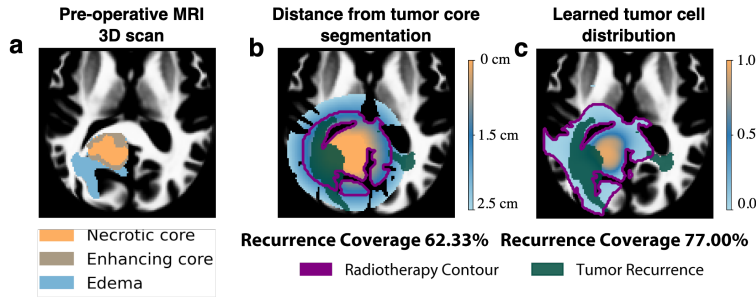


Figure 4: Radiotherapy planning. a) Pre-operative segmentations with white matter concentration as background. b) Distance map from the tumor core segmentation with a 1.5 cm contour and within diffusive tissue, constituting the Standard Plan. c) Our learned tumor cell distribution with the isosurface contour where the enclosed volume equals the total volume of the Standard Plan.

[†]The *Data-Driven Neural Networks (Unconstrained)* is trained end-to-end to predict tumor recurrences from which we extract the radiotherapy volume around it, similar to the distance map (Appendix A).

6.1 Implementation details

Our computational model uses a multi-resolution method [30] with additional, coarser grids to accelerate convergence. We employ four levels of grid refinement, resulting in 152,880,048 unknowns. At the finest grid level of $72 \times 72 \times 72 \times 96$, each grid point contains four unknowns: three for particle positions and one for tumor cell density.

The learning process includes system identification of unknowns: θ_{Dynamics} , θ_{Initial} , and θ_{Imaging} , which parameterize tumor growth dynamics, tissue elasticity, initial conditions, and imaging characteristics. Using the Adam optimizer, convergence takes around 3 hours on an NVIDIA RTX A6000 GPU.

6.2 Dataset

We use a publicly available dataset of 58 patients with preoperative MRI scans and preoperative FET-PET imaging, along with follow-up MRI scans at the first visible tumor recurrence [16] (MIT licence).

6.3 Models and Features

Our analysis includes a range of models, each categorized by their distinct capabilities:

- **Numerical Physics Simulations:** Employ methods such as Finite Element Method (FEM) and Finite Difference Method (FDM) to model tumor growth dynamics and account for dynamic tissue behaviors. The dynamic parameters are determined through numerous simulations with varying parameters. The brain tissues' initial conditions are based on average brains.
- **Data-Driven Neural Networks (Unconstrained):** Use Convolutional Neural Networks (CNNs) to directly predict likely recurrence locations, representing a population-based data-driven approach.
- **Data-Driven Neural Networks (Physics-Constrained):** Similar to the above unconstrained approach but limited to finding parameters for physics simulations, incorporating hard physics constraints.
- **Static Grid Discretization:** A previous state-of-the-art method that uses Optimizing a Discrete Loss (ODIL) and static grids to penalize the learned spatiotemporal tumor cell distribution by quantifying the discrepancy with the tumor growth equation, keeping brain anatomy static throughout the entire process.
- **Standard Plan:** Apply uniform safety margins around the tumor core, serving as the baseline for volume determination and reflecting current clinical practice post-tumor resection surgery radiotherapy planning.

Specific implementations within these categories are explained in Appendix A.

6.4 Results

Table 1, specifically the "Recurrence Coverage [%] (Any)" column, and Figure 5a present results where recurrence is defined by any segmentation visible in the follow-up MRI scan. Our method achieved 74.7% recurrence coverage, surpassing the previous state-of-the-art at 72.9% and the Standard Plan at 70.0%. Using a predefined average brain reduced the performance to 73.4%. The physics-constrained data-driven approach slightly outperforms the Standard Plan at 67.1% and significantly outperforms its unconstrained variant at 59.0%. This highlights the advantage of adding physics constraints. Figure 5a shows the distance between 'Greater' and 'Less' categories increased from 26% to 36%.

Table 1, using the "Recurrence Coverage [%] (Enhancing Core)" column, and Figure 5b show results where recurrence is defined by enhancing core segmentation, per RANO guidelines [31]. Our method leads with 89.9% average recurrence coverage, compared to 89.02% for static grid discretization and 87.3% for the Standard Plan. Numerical physics simulations are more robust at 86.2% compared to 84.31% for the physics-constrained data-driven method. The unconstrained data-driven method

remains the lowest at 66.8%. Results are close because the enhancing core often occurs near pre-operative MRI segmentations, leading to many methods achieving 100% coverage (seen in 'Equal' in Figure 5b). However, Figure 5b shows an increase in the preference from 19% to 28%.

In both recurrence definitions, mean estimate uncertainty is substantial, as Recurrence Coverage for individual patients can vary significantly. These uncertainties are the standard errors of the mean. Nonetheless, Figure 5 shows that even slight improvements in average Recurrence Coverage consistently enhance radiotherapy outcomes compared to the Standard Plan baseline.

Table 1: Comparison of recurrence segmentation coverage given equal radiation volume.

Model	Recurrence Coverage[%] (Any)	Recurrence Coverage[%] (Enhancing Core)	Dynamical Tissues	Inferable Healthy Anatomy	Population-Based Data-Driven	Physics-Constrained
NN (Unconstrained)	59.0 ± 4.3	66.8 ± 4.9	×	×	✓	×
NN (Physics-Constrained)	70.4 ± 3.7	84.3 ± 3.3	×	×	✓	Hard
Numerical Physics Simulations	67.1 ± 3.8	86.2 ± 3.6	✓	×	×	Hard
Standard Plan	70.0 ± 3.8	87.3 ± 3.6	×	×	×	×
Static Grid Discretization	72.9 ± 3.5	89.0 ± 3.3	×	×	×	Soft
Ours (w/o inferable anatomy)*	73.4 ± 3.2	89.3 ± 2.9	✓	×	×	Soft
Ours	74.7 ± 3.1	89.9 ± 2.7	✓	✓	×	Soft

*We set the initial condition for the brain tissues as a hard constraint, representing the average brain.

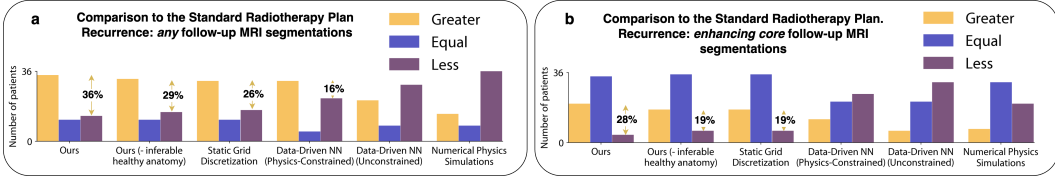


Figure 5: Direct patient-by-patient comparisons to the Standard Plan of radiotherapy plans with equal total volumes. "Greater," "Equal," and "Less" refer to the direct numerical comparison of Recurrence Coverage. a) Recurrence is defined as the union of edema, enhancing core, and necrotic core on the follow-up MRI segmentation. b) Recurrence is defined as the enhancing core on the follow-up MRI segmentation.

7 Conclusion

In this work, we present the first successful approach to a soft-constrained physics system-identification problem that combines the complex biological process of tumor growth with the biomechanical environment such as elastic brain tissues. Our method integrates physics-based constraints with multi-modal imaging data to enhance tumor treatment planning for glioblastomas. The method balances adherence to observed patient data and physics-based penalties through a unique discretization scheme, serving as a flexible spatiotemporal regularization term.

Additionally, our method provides estimates of the initial condition, i.e., tumor-free, pre-deformation anatomy. Such healthy brain anatomy can be utilized in various studies, e.g., for aligning with post-surgical scans to assess the extent of tumor removal and detect complications [32, 33, 34].

Overall, our results show that this approach outperforms previous state-of-the-art techniques in covering tumor recurrence areas, with improved performance on real-world patient data. Finally, we want to point out that relaxing physical model constraints has broad applicability beyond glioblastoma localization. This approach can extend to other real-world problems where rigid physics-based models are limited but still relevant.

Limitations: The convergence speed of the method depends on a multiresolution grid, assuming that problems can be represented at lower resolutions. However, this approach may not be directly applicable to PDEs with narrow-phase interfaces. Additionally, while large deformations are allowed, we assume they are not large enough to cause material rupture, which may not be optimally handled in the Lagrangian perspective without modifications to the presented scheme.

References

- [1] Guido Frosina. Radiotherapy of high-grade gliomas: dealing with a stalemate. *Crit Rev Oncol Hematol*, 190:104110, Oct 2023.
- [2] S. Subramanian, A. Ghafouri, K.M. Scheufele, N. Himthani, C. Davatzikos, and G. Biros. Ensemble inversion for brain tumor growth models with mass effect. *IEEE Trans Med Imaging*, 42(4):982–995, 2023.
- [3] J. Lipkova, P. Angelikopoulos, S. Wu, E. Alberts, B. Wiestler, C. Diehl, C. Preibisch, T. Pyka, S.E. Combs, P. Hadjidoukas, K. Van Leemput, P. Koumoutsakos, J. Lowengrub, and B. Menze. Personalized radiotherapy design for glioblastoma: Integrating mathematical tumor models, multimodal scans, and bayesian inference. *IEEE Trans Med Imaging*, 38(8):1875–1884, 2019.
- [4] Shashank Subramanian and et al. Where did the tumor start? an inverse solver with sparse localization for tumor growth models. *Inverse Problems*, 36(045006), 2020.
- [5] Jonas Weidner, Ivan Ezhov, Michal Balcerak, Marie-Christin Metz, Sergey Litvinov, Sebastian Kaltenbach, Leonhard Feiner, Laurin Lux, Florian Kofler, Jana Lipkova, Jonas Latz, Daniel Rueckert, Bjoern Menze, and Benedikt Wiestler. A learnable prior improves inverse tumor growth modeling, 2024.
- [6] Jens Petersen, Fabian Isensee, Gregor Köhler, Paul F Jäger, David Zimmerer, Ulf Neuberger, Wolfgang Wick, Jürgen Debus, Sabine Heiland, Martin Bendszus, et al. Continuous-time deep glioma growth models. In *Medical Image Computing and Computer Assisted Intervention—MICCAI 2021: 24th International Conference, Strasbourg, France, September 27–October 1, 2021, Proceedings, Part III* 24, pages 83–92. Springer, 2021.
- [7] Ivan Ezhov, Kevin Scibilia, Katharina Frantiza, Felix Steinbauer, Suprosanna Shit, Lucas Zimmer, Jana Lipkova, Florian Kofler, Johannes Paetzold, Luca Canalini, Diana Waldmannstetter, Martin J. Menten, Marie Metz, Benedikt Wiestler, and Bjoern Menze. Learn-morph-infer: a new way of solving the inverse problem for brain tumor modeling. *Medical Image Analysis*, page 102672, 2022.
- [8] Alfredo De Goyeneche Macaya, Shreya Ramachandran, Ke Wang, Ekin Karasan, Joseph Y Cheng, Stella X Yu, and Michael Lustig. Resonet: Noise-trained physics-informed mri off-resonance correction. *Advances in Neural Information Processing Systems*, 36, 2024.
- [9] Ramansh Sharma and Varun Shankar. Accelerated training of physics-informed neural networks (pinns) using meshless discretizations. In S. Koyejo, S. Mohamed, A. Agarwal, D. Belgrave, K. Cho, and A. Oh, editors, *Advances in Neural Information Processing Systems*, volume 35, pages 1034–1046. Curran Associates, Inc., 2022.
- [10] Woojin Cho, Kookjin Lee, Donsub Rim, and Noseong Park. Hypernetwork-based meta-learning for low-rank physics-informed neural networks. In A. Oh, T. Naumann, A. Globerson, K. Saenko, M. Hardt, and S. Levine, editors, *Advances in Neural Information Processing Systems*, volume 36, pages 11219–11231. Curran Associates, Inc., 2023.
- [11] Junwoo Cho, Seungtae Nam, Hyunmo Yang, Seok-Bae Yun, Youngjoon Hong, and Eunbyung Park. Separable physics-informed neural networks. In A. Oh, T. Naumann, A. Globerson, K. Saenko, M. Hardt, and S. Levine, editors, *Advances in Neural Information Processing Systems*, volume 36, pages 23761–23788. Curran Associates, Inc., 2023.
- [12] Aditi Krishnapriyan, Amir Gholami, Shandian Zhe, Robert Kirby, and Michael W Mahoney. Characterizing possible failure modes in physics-informed neural networks. In M. Ranzato, A. Beygelzimer, Y. Dauphin, P.S. Liang, and J. Wortman Vaughan, editors, *Advances in Neural Information Processing Systems*, volume 34, pages 26548–26560. Curran Associates, Inc., 2021.
- [13] Tsung-Yen Yang, Justinian Rosca, Karthik Narasimhan, and Peter J Ramadge. Learning physics constrained dynamics using autoencoders. *Advances in Neural Information Processing Systems*, 35:17157–17172, 2022.

- [14] Karolis Martinkus, Jan Ludwiczak, WEI-CHING LIANG, Julien Lafrance-Vanasse, Isidro Hotzel, Arvind Rajpal, Yan Wu, Kyunghyun Cho, Richard Bonneau, Vladimir Gligorijevic, et al. Abdiffuser: full-atom generation of in-vitro functioning antibodies. In *Thirty-seventh Conference on Neural Information Processing Systems*, 2023.
- [15] Petr Karnakov, Sergey Litvinov, and Petros Koumoutsakos. Solving inverse problems in physics by optimizing a discrete loss: Fast and accurate learning without neural networks. *PNAS Nexus*, 3(1):pgae005, 01 2024.
- [16] Michal Balcerak, Jonas Weidner, Petr Karnakov, Ivan Ezhov, Sergey Litvinov, Petros Koumoutsakos, Ray Zirui Zhang, John S. Lowengrub, Bene Wiestler, and Bjoern Menze. Individualizing glioma radiotherapy planning by optimization of data and physics-informed discrete loss, 2024.
- [17] Ray Zirui Zhang, Ivan Ezhov, Michal Balcerak, Andy Zhu, Benedikt Wiestler, Bjoern Menze, and John Lowengrub. Personalized predictions of glioblastoma infiltration: Mathematical models, physics-informed neural networks and multimodal scans, 2024.
- [18] Ben Mildenhall, Pratul P Srinivasan, Matthew Tancik, Jonathan T Barron, Ravi Ramamoorthi, and Ren Ng. Nerf: Representing scenes as neural radiance fields for view synthesis. In *European Conference on Computer Vision*, pages 405–421. Springer, 2020.
- [19] Xuan Li, Yi-Ling Qiao, Peter Yichen Chen, Krishna Murthy Jatavallabhula, Ming Lin, Chenfanfu Jiang, and Chuang Gan. PAC-neRF: Physics augmented continuum neural radiance fields for geometry-agnostic system identification. In *The Eleventh International Conference on Learning Representations*, 2023.
- [20] Bernhard Kerbl, Georgios Kopanas, Thomas Leimkühler, and George Drettakis. 3d gaussian splatting for real-time radiance field rendering. *ACM Transactions on Graphics*, 42(4):1–14, 2023.
- [21] Cheng Sun, Min Sun, and Hwann-Tzong Chen. Direct voxel grid optimization: Super-fast convergence for radiance fields reconstruction. In *Proceedings of the IEEE/CVF Conference on Computer Vision and Pattern Recognition*, pages 5459–5469, 2022.
- [22] Federica Caforio, Francesco Regazzoni, Stefano Pagani, Elias Karabelas, Christoph Augustin, Gundolf Haase, Gernot Plank, and Alfio Quarteroni. Physics-informed neural network estimation of material properties in soft tissue nonlinear biomechanical models, 2023.
- [23] Arunabha M. Roy and Rikhi Bose. Physics-aware deep learning framework for linear elasticity, 2023.
- [24] S. Subramanian, A. Gholami, and G. Biros. Simulation of glioblastoma growth using a 3d multispecies tumor model with mass effect. *J Math Biol*, 79(3):941–967, 2019.
- [25] Raymond W. Ogden. *Non-linear Elastic Deformations*. Dover Publications, Mineola, New York, 1997.
- [26] Arthur W. Toga and Paul M. Thompson. Mapping brain asymmetry. *Nature Reviews Neuroscience*, 4(1):37–48, 2003.
- [27] Meng-Chuan Lai et al. A shift to randomness of brain oscillations in people with autism. *Biological Psychiatry*, 71(5):410–417, 2012.
- [28] Florian Kofler, Christoph Berger, Diana Waldmannstetter, Jana Lipkova, Ivan Ezhov, Giles Tetteh, Jan Kirschke, Claus Zimmer, Benedikt Wiestler, and Bjoern H Menze. Brats toolkit: translating brats brain tumor segmentation algorithms into clinical and scientific practice. *Frontiers in neuroscience*, page 125, 2020.
- [29] Jana Lipková, Panagiotis Angelikopoulos, Stephen Wu, Esther Alberts, Benedikt Wiestler, Christian Diehl, Christine Preibisch, Thomas Pyka, Stephanie E Combs, Panagiotis Hadjidoukas, et al. Personalized radiotherapy design for glioblastoma: Integrating mathematical tumor models, multimodal scans, and bayesian inference. *IEEE transactions on medical imaging*, 38(8):1875–1884, 2019.

- [30] Petr Karnakov, Sergey Litvinov, and Petros Koumoutsakos. Flow reconstruction by multiresolution optimization of a discrete loss with automatic differentiation. *The European Physical Journal E*, 46(7):59, Jul 2023.
- [31] Benjamin M. Ellingson, Patrick Y. Wen, and Timothy F. Cloughesy. Modified criteria for radiographic response assessment in glioblastoma clinical trials. *Neurotherapeutics*, 14(2):307–320, Apr 2017.
- [32] Adam T Kessler and Ami A Bhatt. Brain tumour post-treatment imaging and treatment-related complications. *Insights into Imaging*, 9(6):1057–1075, Dec 2018. Epub 2018 Nov 8.
- [33] Barbara Kiesel, Romana Prihoda, Martin Borkovec, Petra A. Mercea, Ariane Steindl, Anna S. Berghoff, Julia Furtner, Johannes Leitner, Thomas Roetzer, Matthias Preusser, Karl Roessler, and Georg Widhalm. Postoperative magnetic resonance imaging after surgery of brain metastases: Analysis of extent of resection and potential risk factors for incomplete resection. *World Neurosurgery*, 143:e365–e373, 2020.
- [34] Michael W. Gerber et al. Assessing the extent of resection in glioma surgery using intraoperative mri and functional mapping. *Journal of Neurosurgery*, 128(1):87–98, 2018.
- [35] S. Subramanian, A. Gholami, and G. Biros. Simulation of glioblastoma growth using a 3d multispecies tumor model with mass effect. *Journal of Mathematical Biology*, 79:941–967, 2019.
- [36] Sergio M. Martin, Daniel Wälchli, Georgios Arampatzis, Athena E. Economides, Petr Karnakov, and Petros Koumoutsakos. Korali: Efficient and scalable software framework for bayesian uncertainty quantification and stochastic optimization. *Computer Methods in Applied Mechanics and Engineering*, 389:114264, 2022.
- [37] Fabian Isensee, Paul F. Jaeger, Simon A. A. Kohl, Jens Petersen, and Klaus H. Maier-Hein. nnu-net: a self-configuring method for deep learning-based biomedical image segmentation. *Nature Methods*, 18:203–211, 2021.
- [38] Michael Weller. Eano guidelines on the diagnosis and treatment of diffuse gliomas of adulthood. *Nature Reviews Clinical Oncology*, 18:170–186, 2021.
- [39] M. Niyazi, N. Andratschke, M. Bendszus, A.J. Chalmers, S.C. Erridge, N. Galldiks, et al. Estro-eano guideline on target delineation and radiotherapy details for glioblastoma. *Radiother Oncol*, 2023.

A Baselines Implementation

Here we provide details regarding the specific baseline implementations:

Numerical Physics Simulations : We employ the numerical forward simulation scheme from [35] which was implemented on GPU [7]. The simulations follows the equation 1. We initialize the brain tissues with a rigidly registered average brain. For θ_{Dynamics} , $x_0 \in \theta_{\text{Initial}}$, and θ_{Imaging} , we use the Covariance Matrix Adaptation Evolution Strategy (CMA-ES) method [5, 36].

Data-Driven Neural Networks (Unconstrained) : We use nnU-Net [37] which takes brain tissue distribution, FET-PET map, and pre-operative tumor segmentations to directly predict core tumor recurrences. After predicting the recurrences, we construct a distance distribution from the predicted recurrences. This distribution is then thresholded, similar to other methods, to create a binary radiotherapy treatment map of the same volume as the Standard Plan. The network is trained using an 80%/20% train-test split.

Data-Driven Neural Networks (Physics Constrained) : We employ a recently published method [7] that uses CNNs to map pre-operative tumor segmentation to θ_{Dynamics} and runs a numerical simulation following equation 1. This method uses an average brain as the initial condition. After inference, the tumor cell distribution is non-rigidly registered to the patient’s brain anatomy.

Static Grid Discretization : This method, as implemented in [16], uses estimated brain tissues (4) as the initial condition for the anatomy and later keeps the tissues static, effectively setting $\gamma \in \theta_{\text{Dynamics}}$ in Equation 3 to 0.

Standard Plan : This approach uses a 1.5 cm uniform safety margin around the resection cavity and/or remaining tumor on MRI imaging, aligning with both North American and European guidelines [38, 39].

B Imaging Model

The core of the method's alignment with the data is encapsulated by the loss function components, which associate the simulated outputs with key imaging traits such as the tumor core, surrounding edema, metabolic activity detected through FET-PET imaging, and visible brain tissues. This loss function depends on two learnable parameters $\theta_{\text{Imaging}} = \{\theta_{\text{down}}, \theta_{\text{up}}\}$ and is expressed as:

$$L_{\text{Visible Data}} = \alpha_6 L_{\text{Core}}(c, \theta_{\text{up}}) + \alpha_7 L_{\text{Edema}}(c, \theta_{\text{down}}, \theta_{\text{up}}) + \alpha_8 L_{\text{Metabolic Map}}(c) + \alpha_9 L_{\text{Tissues}}(\mathbf{m}) \quad (11)$$

The loss function is composed of individual terms corresponding to distinct anatomical features:

- L_{Core} relates tumor cell concentrations above the threshold θ_{up} to the tumor core region.
- L_{Edema} delineates the edema area surrounding the tumor, regulated by the lower and upper thresholds θ_{down} and θ_{up} .
- $L_{\text{Metabolic Map}}$ assesses the metabolic activity as indicated by FET-PET signals within the edema and core regions, using a simple correlation metric, L_{Tissues} connects visible brain tissues with those inferred by the method.

These adaptive parameters $\{\theta_{\text{down}}, \theta_{\text{up}}\}$ enable the model to accommodate variations in MRI/FET-PET imaging contrasts and noise levels.

We adopt sigmoid functions to portray the gradational transitions observed at tumor region margins. The sigmoid, $\sigma(x)$, is specified as:

$$\sigma(x) = \frac{1}{1 + e^{-\beta x}} \quad (12)$$

Here, β modulates the steepness of the transition and is set to $\beta = 50$. For the tumor core:

$$L_{\text{Core}}(c, \theta_{\text{up}}) = \sum_{i=0}^{N_x} \sigma(\theta_{\text{up}} - c_i^{N_t} - \alpha) \quad (13)$$

for the edema:

$$L_{\text{Edema}}(c, \theta_{\text{down}}, \theta_{\text{up}}) = \sum_{i=0}^{N_x} \sigma(\theta_{\text{down}} - u_i^{N_t} - \alpha) + (1 - \sigma(\theta_{\text{up}} - c_i^{N_t} + \alpha)) \quad (14)$$

where α offsets the thresholds and is set to $\alpha = 0.05$.

In this context, Ω_2 represents the collection of voxels that map to the time point at which the imaging is conducted; for single-image analysis, this corresponds to the final time slice.

The metabolic activity within the tumor is evaluated by the loss term L_{PET} , which measures the correlation between the simulated metabolic signal and actual FET-PET scan observations:

$$L_{\text{PET}}(c) = 1 - \text{corr}(c^{N_t}, p^{\text{PET}}) \quad (15)$$

Here, $\text{corr}(u^n, p^{\text{PET}})$ represents the Pearson correlation coefficient between the predicted tumor cell densities c^{N_t} and the restricted FET-PET signal p^{PET} , across all voxels within the edema and enhancing core regions, providing a direct measure of how well the model predictions align with the observed metabolic profiles.

C Assumption of Brain Symmetry at Initial Time Without the Tumor

Our model employs a multi-resolution analysis to assess brain symmetry, particularly useful since the brain’s symmetry is more evident at coarser resolutions. This approach is applied to key tissue types: white matter (WM), gray matter (GM), and cerebrospinal fluid (CSF), each analyzed at full, 2x, and 4x downsampled levels to accommodate both the brain’s structural nuances and computational efficiency.

The process for each tissue type involves converting tissue data into particles, then calculating symmetry loss at each resolution. This calculation entails:

1. Downsample the tissue representation, using average pooling
2. Divide the tissue’s downsampled representation along its height, reflecting the brain’s hemispherical division.
3. Mirror one hemisphere and compare it to the other, quantifying symmetry by calculating the mean absolute difference between them.

The total symmetry loss (L) accumulates across all tissues and resolutions to measure deviation from an ideal symmetric state:

$$L_{\text{Healthy Brain}}(\mathbf{m}) = \sum_{k=1}^3 \sum_{\kappa=0}^2 \text{calculate_symmetry_loss}(m_k, \text{scale_factor} = 2^\kappa) \quad (16)$$

The multi-resolution approach not only addresses the limitations of assuming brain symmetry at detailed levels but also streamlines computational efforts. The smoother landscape at downsampled resolutions is especially favorable for particle movement through gradient descent.

D Synthetic Experiments

To calibrate the loss function weights, we generated a synthetic dataset for single focal and localized multi-focal tumors by solving PDEs using a finite difference method numerical solver [7]. An average brain model was used to represent the spatial distribution of brain tissues. Tumor growth model parameters, elasticity, imaging model parameters, and 1 or 3 focal locations were varied using uniform random distributions. A fixed seed was used for reproducibility.

The metric used was the RMSE between the learned and ground truth tumor cell distributions. In total, 100 synthetic patients were generated. Table 2 provides the details of the parameter ranges used for generating the synthetic single focal and multi-focal tumor datasets.

Table 2: Parameter ranges for generating synthetic single focal and multi-focal tumor datasets

Shared parameters		
Parameter	Min	Max
D_w	0.035	0.2
ρ	0.035	0.2
R	10	30
θ_{necro}	0.70	0.85
θ_{up}	0.45	0.60
θ_{down}	0.15	0.35
T_{sim}	100	
Single focal tumor center (mm)		
(x_0, y_0, z_0)	57.6	96
Multi-focal tumor centers (mm)		
Tumor 1 center (x_0^1, y_0^1, z_0^1)	57.6	96
Tumor 2 center (x_0^2, y_0^2, z_0^2)	$(x_0^1, y_0^1, z_0^1) \pm 9.6$	
Tumor 3 center (x_0^3, y_0^3, z_0^3)	$(x_0^2, y_0^2, z_0^2) \pm 9.6$	

E Material Parameters for Biological Tissues

The table below summarizes the Young’s modulus and Poisson’s ratio for different tissue types used in the hyperelastic modeling of biological tissues.

Tissue Type	Young’s Modulus (Pa)	Poisson’s Ratio
Grey Matter (GM)	2100	0.4
White Matter (WM)	2100	0.4
Cerebrospinal Fluid (CSF)	100	0.1
Tumor	8000	0.45

Table 3: Young’s modulus and Poisson’s ratio for biological tissues.